Acta Materialia 262 (2024) 119460

Contents lists available at ScienceDirect

Acta Materialia

journal homepage: www.elsevier.com/locate/actamat

Full length article

Empirical interatomic potentials for ZrO_2 and YSZ polymorphs: Application to a tetragonal ZrO_2 grain boundary

Susumu Fujii [a,b,*], Katsuhiko Shimazaki [a], Akihide Kuwabara [b,c]

[a] Division of Materials and Manufacturing Science, Osaka University, Suita, Osaka 565-0871, Japan
[b] Nanostructures Research Laboratory, Japan Fine Ceramics Center, Atsuta, Nagoya 456-8587, Japan
[c] Next Generation Zirconia Social Cooperation Program, Institute of Engineering Innovation, The University of Tokyo, Bunkyo-ku, Tokyo 113-8656, Japan

ARTICLE INFO

Keywords:
Zirconia polymorphs
Yttria stabilized zirconia
Interatomic potentials
Molecular dynamics
Grain boundary

ABSTRACT

Yttria stabilized zirconia (YSZ) ceramics have been used for various engineering applications including structural ceramics, biomedical materials, and thermal barrier coatings. The versatile and excellent properties of YSZ stem from its unique microstructure consisting of monoclinic, tetragonal, and cubic phases, whose stability depends on yttria concentration and temperature. However, there are no empirical interatomic potentials (EIPs) that can reproduce the structures and energies of ZrO_2 and YSZ polymorphs, limiting the atomic-scale investigation of lattice defect structures and their interactions that affect the YSZ microstructure and properties. Here, using a genetic algorithm and *ab initio* training datasets, we have optimized EIPs to sufficiently reproduce the structures and stability of ZrO_2 and YSZ polymorphs, as well as the properties of the tetragonal and cubic phases at finite temperature. The potentials have also been applied to the search for a tetragonal grain boundary structure, showing that the obtained grain boundary structure is consistent with that obtained by *ab initio* calculations. The developed EIPs will aid in revealing the microstructure-property relationships in YSZ by performing large-scale and systematic calculations, which are practically difficult to perform with *ab initio* and machine-learning-potential calculations.

1. Introduction

Zirconia ceramics, denoted by the chemical formula ZrO_2, have been used for a variety of applications, including structure ceramics, biomedical materials, thermal barrier coatings, and solid electrolytes in solid oxide fuel cells [1–6]. Pure ZrO_2 exists as a monoclinic phase ($P2_1/c$) at room temperature, but transforms to tetragonal ($P4_2/nmc$) and cubic ($Fm\text{-}3m$) phases at higher temperatures [7–9]. The most important phases for engineering are the tetragonal and cubic phases, which are stabilized by cations with ionic radii larger than Zr^{4+} and/or cations with lower valences than Zr^{4+} that create oxide-ion vacancies for charge neutrality [9–11]. The most widely used dopant for ZrO_2 is yttria (Y_2O_3), and Y_2O_3-doped ZrO_2 is called as yttria-stabilized zirconia (YSZ) [1–5].

The versatile and excellent properties of YSZ originate from their dopant concentration and microstructure [2]. YSZ with 2-4 mol% Y_2O_3, called as yttria stabilized tetragonal zirconia polycrystal (Y-TZP), exhibits high strength and toughness simultaneously [12]. Y-TZP is actually a tetragonal-cubic dual phase, with the fraction of tetragonal phase of 80-100% [13]. The tetragonal-to-cubic phase transformation is induced by the grain boundary (GB) segregation of Y^{3+} ions during annealing [2,13]. The high toughness of Y-TZP is due to the tetragonal-to-monoclinic phase transformation, which is accompanied by a volume expansion of ~4% and suppresses crack propagation [14]. For thermal barrier coating applications, the Y_2O_3 composition ranges from 3.9 to 4.5 mol%, slightly higher than Y-TZP [15,16]. This is to avoid the tetragonal-to-monoclinic phase transformation because the volume change causes the spallation of the coating system. The addition of 8-10 mol% Y_2O_3 results in a fully cubic YSZ [9] with a high concentration of oxide-ion vacancies and a highly symmetric structure, resulting in high oxide-ion conductivity. Even in this case, the performance varies significantly depending on the microstructure with different distributions of yttrium ions [17].

The microstructure of ZrO_2 and YSZ, such as GB atomic structure, GB segregation of Y, and their impacts on material properties, has been the subject of computational studies using empirical interatomic potentials (EIPs) [18–22], in conjunction with experimental observations using transmission electron microscopy (TEM) [23–25]. However, the

* Corresponding author.
E-mail address: susumu.fujii@mat.eng.osaka-u.ac.jp (S. Fujii).

https://doi.org/10.1016/j.actamat.2023.119460
Received 6 September 2023; Received in revised form 20 October 2023; Accepted 21 October 2023
Available online 22 October 2023

computational research has mainly focused on cubic YSZ, leaving a limited understanding of the microstructure of tetragonal and tetragonal-cubic dual phases. This is due to the lack of computationally inexpensive interatomic potentials that can sufficiently reproduce a variety of ZrO_2 and YSZ polymorphs, including the monoclinic, tetragonal, and cubic phases. While *ab initio* calculations can accurately reproduce the structural features of ZrO_2 polymorphs [26,27], it is unfortunately difficult to investigate the large number of lattice defect structures associated with Y_2O_3 dopant in a realistic time.

Recently, machine learning potentials (MLPs) have been developed for ZrO_2 and ZrO_2-Y_2O_3 system, which were trained with the data generated by *ab initio* calculations [28–32]. Verdi *et al.* reported MLPs that can reproduce the monoclinic, tetragonal, and cubic ZrO_2 structures and the monoclinic-to-tetragonal, and tetragonal-to-cubic phase transformations with high accuracy [28,29]. Guan *et al.* developed an MLP for $Y_{2x}Zr_{1-x}O_{2-x}$ and investigated their structural features and effects on oxide-ion conductivity [31,32]. Although their applicability to lattice defect structures has not been verified, the development of these MLPs will be useful for revealing the YSZ microstructure and its influence on mechanical, thermal, and ionic conduction properties [33]. However, while MLPs are several orders of magnitude faster than *ab initio* calculations, they are several orders of magnitude slower than EIPs due to their highly flexible but complex functional form [34,35]. EIPs that can reproduce ZrO_2 and YSZ polymorphs are still necessary to systematically and statistically investigate the YSZ microstructure, which contains a large number of lattice defects.

A few EIPs have been developed to reproduce the structures and properties of ZrO_2 polymorphs. Atomic interactions in ZrO_2 are often described by Coulomb-Buckingham interatomic potentials, which are commonly used for ionic materials [36,37]. Bandura *et al.* reported EIPs that combine Coulomb-Buckingham potential with inverse Gaussian, Fermi-Dirac, and Morse potentials [38]. The developed EIPs successfully reproduce the structures and energies of monoclinic, tetragonal, cubic, and also high-pressure orthorhombic I and II phases [39] in static calculations. However, the applicability of their EIPs to the dynamical behaviors of ZrO_2 at finite temperatures such as phase transformations and thermal expansion, and to the defect configuration such as tetragonal grain boundary structures, has not been investigated. The interatomic potential for yttrium ions has also not been developed, making the computational approach to YSZ polymorphs and microstructures impossible.

To address these issues, we have developed EIPs that can simulate the ZrO_2 and YSZ polymorphs and their properties at finite temperature. Their potential parameters were optimized by a genetic algorithm [40] to reproduce a variety of data generated by *ab initio* calculations. The genetic algorithm optimized potentials (GAOPs) can reproduce monoclinic, tetragonal, cubic, orthorhombic I and II, and other hypothetical ZrO_2 structures and their stability. In particular, they are capable of reproducing the properties of the tetragonal and cubic phases, which are of great engineering importance. The high temperature stability of the tetragonal phase, the tetragonal-to-cubic phase transformation, and the Y_2O_3 concentration dependence of the tetragonal and cubic phase stability are in good agreement with experiments. In addition, the tetragonal GB structure derived using GAOPs is found to be consistent with that of *ab initio* calculations. The developed GAOPs will accelerate our understanding of the ZrO_2 and YSZ microstructures, including the tetragonal GB structures, Y segregation at GBs, and their impact on material properties, in combination with more accurate MLP-based and *ab initio* calculations.

2. Methods

2.1. Interatomic potentials

In this study, interatomic potentials for Zr-Y-O system are defined as follows according to Bandura *et al.* [38]:

Table 1
Parameter ranges of interatomic potentials and their optimal values for GAOP1.

	Parameter	Range	Optimized value
Charge	q (e)	0.500 - 1.000	0.511
Zr-Zr	A^{Gauss} (eV)	-1.000 - 1.000	0.125
	B^{Gauss} (Å^{-1})	0.200 - 10.000	9.228
	r_0^{Gauss}(Å)	2.500 - 5.000	3.281
Zr-O	A^{Buck} (eV)	100.00 - 20000.00	15026.89
	ρ^{Buck} (Å)	0.1000 - 0.5000	0.1969
	C^{Buck} (eVÅ^6)	Fixed	5.1
	A^{Gauss} (eV)	-1.000 - 1.000	0.677
	B^{Gauss} (Å^{-1})	0.200 - 10.000	1.902
	r_0^{Gauss}(Å)	1.500 - 3.500	2.187
	A^{Fermi} (eV)	-5.000 - 0.000	-0.647
	B^{Fermi} (Å^{-1})	0.500 - 5.000	2.467
	r_0^{Fermi}(Å)	1.500 - 3.500	1.626
O-O	A^{Buck} (eV)	100.00 - 20000.00	3207.39
	ρ^{Buck} (Å)	0.1000 - 0.5000	0.2993
	C^{Buck} (eVÅ^6)	Fixed	32.0
Y-O	A^{Buck} (eV)	100.00 - 20000.00	1809.00
	ρ^{Buck} (Å)	0.0100 - 0.5000	0.2714
	C^{Buck} (eVÅ^6)	1.000 - 100.000	14.374

Table 2
Parameter ranges of interatomic potentials and their optimal values for GAOP2. In addition to the parameters of GAOP1 shown in Table 1, Zr-Zr Buckingham and Fermi-Dirac potentials are included, and the Y-O Buckingham potential is modified from GAOP1.

	Parameter	Range	Optimized value
Charge	q (e)	0.500 - 1.000	0.511
Zr-Zr	A^{Buck} (eV)	1.00 - 30000.00	15555.86
	ρ^{Buck} (Å)	0.1000 - 0.5000	0.2674
	C^{Buck} (eVÅ^6)	0.01 - 200.00	78.63
	A^{Fermi} (eV)	-1.000 - 1.000	0.087
	B^{Fermi} (Å^{-1})	0.500 - 10.000	8.704
	r_0^{Fermi}(Å)	2.500 - 6.000	4.710
Y-O	A^{Buck} (eV)	1.00 - 30000.00	2027.32
	ρ^{Buck} (Å)	0.0100 - 0.5000	0.2678
	C^{Buck} (eVÅ^6)	0.010 - 200.000	15.830

$$\Phi_{ij}(r_{ij}) = \Phi_{ij}^{Buck} + \Phi_{ij}^{Gauss} + \Phi_{ij}^{Fermi} + \Phi_{ij}^{Coulomb} \quad (1)$$

$$\Phi_{ij}^{Buck}(r_{ij}) = A_{ij}^{Buck}\exp\left(-\frac{r_{ij}}{\rho_{ij}^{Buck}}\right) - \frac{C_{ij}^{Buck}}{r_{ij}^6}, \quad (2)$$

$$\Phi_{ij}^{Gauss}(r_{ij}) = -A_{ij}^{Gauss}\exp\left[-B_{ij}^{Gauss}\left(r_{ij} - r_{0,\,ij}^{Gauss}\right)^2\right], \quad (3)$$

$$\Phi_{ij}^{Fermi}(r_{ij}) = \frac{A_{ij}^{Fermi}}{1+\exp\left[B_{ij}^{Fermi}\left(r_{ij} - r_{0,\,ij}^{Fermi}\right)\right]}, \quad (4)$$

$$\Phi_{ij}^{Coulomb}(r_{ij}) = \frac{q_i q_j}{4\pi\varepsilon_0 r_{ij}}, \quad (5)$$

where Φ_{ij} and r_{ij} are the potential energy and distance of atoms i and j. Φ_{ij}^{Buck}, Φ_{ij}^{Gauss}, and Φ_{ij}^{Fermi} are the short-range interatomic potentials in the form of Buckingham, inverted Gaussian, and Fermi-Dirac. A, B, C, ρ, and r_0 are the parameters of the short-range potentials. $\Phi_{ij}^{Coulomb}$ is the long-range Coulombic potential. q_i and q_j are the effective charges of atoms i and j, and ε_0 is the vacuum permittivity. To maintain the charge neutrality, the effective charges of Zr, O, and Y were defined as proportional to q as $4q$, $-2q$, and $3q$, reflecting ratios of their formal charges. The cutoff distance for short-range potentials was set to 12.0 Å. The parameter ranges considered in the genetic algorithm optimizations are listed in Tables 1 and 2.

2.2. Datasets

Two EIPs for ZrO_2 and YSZ polymorphs were generated by a genetic algorithm, namely GAOP1 and GAOP2. GAOP2 is the modified version of GAOP1 to improve the reproducibility of various crystal structures.

The training dataset for GAOP1 includes (1) relative energies, lattice constants, and atomic positions of monoclinic, tetragonal, cubic, orthorhombic I and II phases (brookite and cotunnite) and one hypothetical ZrO_2 structure that often appeared in our preliminary parameter fitting trials (hy-ZrO_2), (2) lattice constants and atomic positions of Y_2O_3 phase, (3-5) relative energies, forces acting on atoms, and stresses in (3) respective 50 deformed models of tetragonal and cubic ZrO_2, (4) 100 configurations of tetragonal ZrO_2 at 1000 K obtained by *ab initio* molecular dynamics (MD) simulations, and (5) respective 50 deformed models of 3 mol% Y_2O_3 tetragonal YSZ (3YSZ) and 10 mol% Y_2O_3 cubic YSZ (10YSZ). For (1-2), the conventional unit cells of ZrO_2 polymorphs and Y_2O_3 were used. For (3-5), cubic ZrO_2 supercells of 2×2×2 conventional unit cells and tetragonal ZrO_2 supercells of similar size were constructed. 32 Zr and 64 O ions are contained in the supercells with a lattice parameter a of approximately 10 Å. 3YSZ models were constructed by randomly replacing 2 Zr atoms with Y atoms ($2Y_{Zr}$) and introducing 1 oxygen vacancy (V_O) in the tetragonal ZrO_2 supercell. In case of 10YSZ, $6Y_{Zr}$ and $3V_O$ are introduced into the cubic ZrO_2 supercell. In 3YSZ and 10YSZ, twenty and two models with random Y_{Zr} and V_O configurations were constructed for the training and test datasets, respectively.

The training dataset for GAOP2 is the same for GAOP1 except for (1). The training for GAOP2 considers relative energies, lattice constants, and atomic positions of 19 different polymorphs, namely monoclinic, tetragonal, cubic, orthorhombic I and II, hy-ZrO_2, and 13 other structures found in Materials Project database (mp-556605, 754403, 754741, 755089, 755759, 755769, 775909, 775910, 775935, 775980, 776386, 776404, and 776427) [41]. The lattice parameters and atomic positions of ZrO_2 polymorphs, 3YSZ, and 10YSZ models were optimized so that the atomic residual forces were less than 1.0×10^{-2} eVÅ^{-1}.

Structural deformations, *i.e.*, random lattice distortion and atomic displacements, were introduced into each tetragonal and cubic ZrO_2, and 3YSZ and 10 YSZ model according to Seko *et al.* [42]:

$$\boldsymbol{A}' = \boldsymbol{A} + \varepsilon_A \boldsymbol{R}, \tag{6}$$

$$\boldsymbol{f}' = \boldsymbol{f} + \varepsilon_f \boldsymbol{A}'^{-1} \boldsymbol{\eta}, \tag{7}$$

where $\boldsymbol{A}$ and $\boldsymbol{A}'$ are the lattice vectors of the supercell. $\boldsymbol{f}$ and $\boldsymbol{f}'$ are the fractional coordinates of the atoms in the supercell. $\boldsymbol{R}$ and $\boldsymbol{\eta}$ are a (3×3) matrix and a three-dimensional vector, respectively, that contains random numbers between -1 and 1 and introduces lattice distortion and atomic displacements. ε_A and ε_f control the magnitude of the lattice distortion and atomic displacements. For tetragonal and cubic ZrO_2, 50 deformations were generated for training and 5 for testing. For 3YSZ and 10YSZ, 5 deformations were generated for each model. The values of ε_A and ε_f for the Nth distortion and displacements were set to $\varepsilon_A = 0.250\ N/N_{\text{total}}$ Å and $\varepsilon_f = 0.125\ N/N_{\text{total}}$ Å to include various deformations.

Ab initio MD simulations for a tetragonal supercell were performed for 14 ps with a timestep of 2 fs (7000 steps). The isothermal-isobaric (NPT) ensemble was employed with Langevin thermostat and Parrinello-Rahman barostat. The target temperature and pressure were set to 1000 K and 0 GPa. From MD simulations, 100 (10) atomic configurations at 50-step intervals from 1550 to 6500 steps (from 6550 to 7000 steps) were extracted and used for the training (test) data.

All *ab initio* calculations were performed using density functional theory (DFT) calculations with the plane-wave basis projector augmented wave (PAW) method [43] as implemented in the Vienna *Ab initio* Simulation Package (VASP) [44,45]. The computational conditions are the same for structure optimization, energy, force, and stress evaluation, and MD simulation. The generalized gradient approximation (GGA) in the form of PBEsol [46] was employed. The plane-wave energy cutoff was set to 500 eV. The total energy convergence was set to 1.0×10^{-6} eV/cell. The first Brillouin zone was sampled with Monkhorst-Pack k-point grids [47] with a grid spacing of 0.4 Å^{-1} (2×2×2 grids for the supercells). The PAW potentials used in this study have the following valence configurations: [$4s^2\ 4p^6\ 5s^2\ 4d^2$] for Zr, [$4s^2\ 4p^6\ 5s^2\ 4d^1$] for Y, and [$2s^2\ 2p^4$] for O. The rest electrons were treated as fixed core electrons.

2.3. Fitting process of potential parameters

We firstly explain the details of GAOP1. Our fitting process can be divided into two steps, one for the potentials of ZrO_2 and one for an additional Y-O interaction. In the first step, the effective atomic charges, and potential parameters for Zr-O (Buckingham, Gaussian, Fermi-Dirac), O-O (Buckingham), and Zr-Zr (Gaussian) interactions were optimized by a genetic algorithm. The first training dataset contains the data (1, 3, 4) as described in subsection 2.2. In the second step, the potential parameters for Y-O (Buckingham) were optimized. The second training dataset contains the data (2, 5) as described in subsection 2.2.

The fitting process of GAOP2 was also divided into two steps. First, Zr-Zr potentials in the form of Buckingham and Fermi-Dirac were added to GAOP1, with the other parameters fixed. The data (1) were changed to include a larger number of crystal structures as described in subsection 2.2, and the additional potential parameters for Zr-Zr interaction were optimized. Then, Y-O Buckingham potential parameters were refitted with the modified Zr-Zr interatomic potentials as the second step. The training dataset was the same with those used in the second fitting of GAOP1.

2.4. Genetic algorithm

We employed the code POPs [40], which utilizes a genetic algorithm to optimize empirical potentials. The genetic algorithm generates N_p individuals with random genotypes representing potential parameters, evaluate the fitness of the individuals by the objective function Z, and searches for the optimal genotypes with low Z by repeating the generation N_g times while recombining and mutating the genotypes of individuals. See the reference for more details [40]. 5% of the superior individuals were passed into the next generation. The rate of mutation was set to 40% to reduce the probability of the potential parameters into local minima. N_p and N_g were set to 1000. In the second fitting for the Y-O interaction, the search was terminated after a few to several dozen generations because there were only three parameters to optimize and the objective function Z rapidly converged. The first and second fittings were performed 200 times and 20 times, respectively, in GAOP1, and both 40 times in GAOP2, using different initial populations with random genotypes.

We defined the objective function Z as follows:

$$Z = Z_{e1} + Z_l + Z_p + Z_{e2} + Z_f + Z_s, \tag{8}$$

where Z_{e1}, Z_l, and Z_p are the errors of relative energy, lattice constant, and fractional coordinate of ZrO_2 polymorphs, estimated from the training data (1-2). Z_{e2}, Z_f, and Z_s are the errors of relative energy, force, and stress of deformed ZrO_2 and YSZ models, estimated from the training data (3-5). The energies, lattice constants, fractional coordinates, forces, and stresses of EIPs were calculated using the Large-scale Atomic/Molecular Massively Parallel Simulator (LAMMPS) [48]. To calculate the above objective function Z, the POPs code was slightly modified by the author.

Z_{e1}, Z_l, and Z_p are the functions for reproducing the crystal structures of ZrO_2 polymorphs and Y_2O_3 and are defined as follows:

$$Z_{e1} = \sum_i^{M_1} w_{e1i} \left(E_i^{\text{DFT}} - E_i^{\text{EIP}}\right)^2, \tag{9}$$

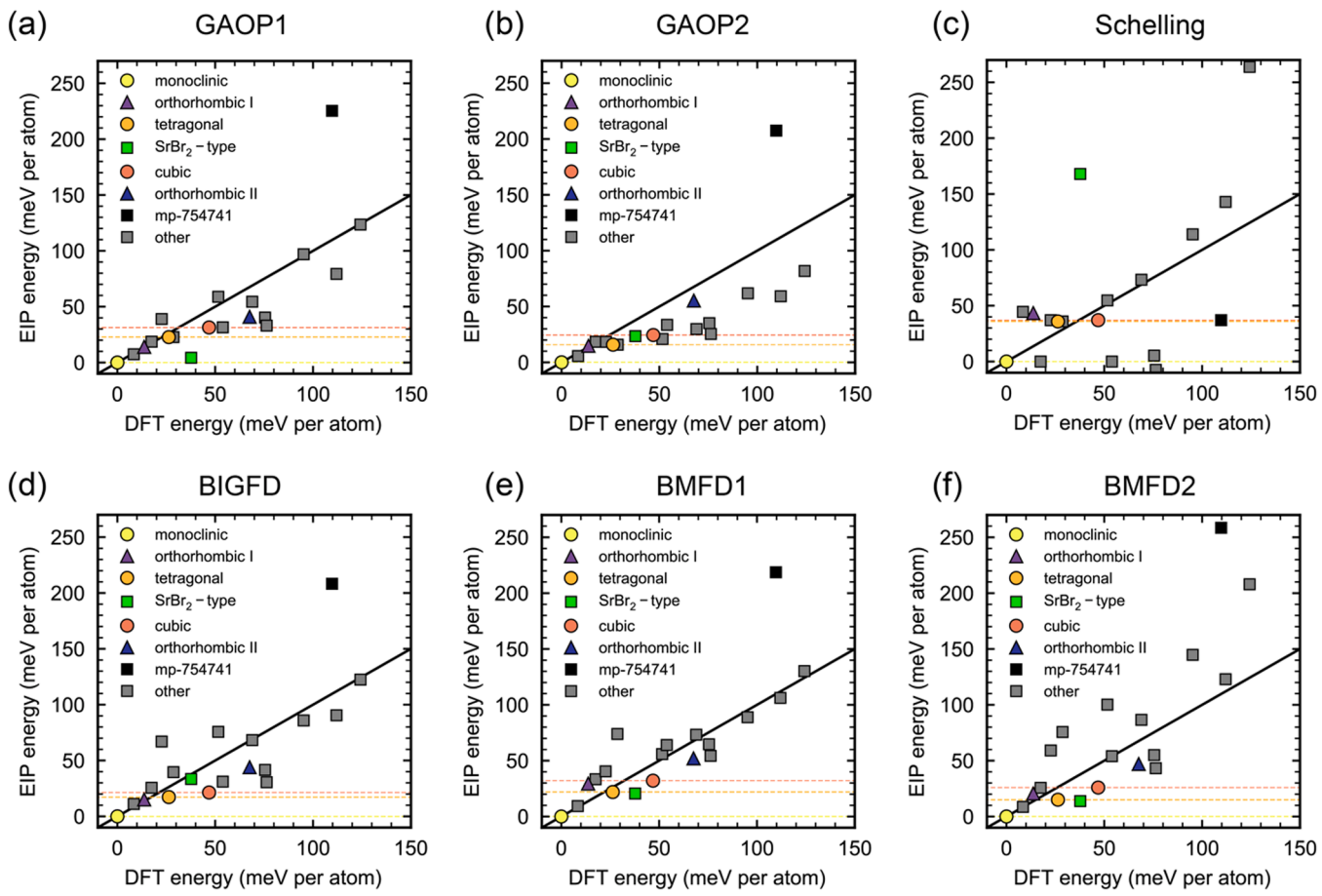

Fig. 1. Comparison of EIP and DFT energies for 19 ZrO_2 polymorphs with six different EIPs. The energies are referenced to that of the monoclinic phase obtained with each calculation condition. (a, b) The developed (a) GAOP1 and (b) GAOP2. (c) The EIPs reported by Schelling et al. [37] (d-f) The EIPs reported by Bandura et al. [38], namely (d) BIGFD, (e) BMFD1, and (f) BMFD2.

$$Z_l = \sum_i^{M_1} w_{li} \sum_j^{6} \left(l_{ij}^{\mathrm{DFT}} - l_{ij}^{\mathrm{EIP}} \right)^2, \tag{10}$$

$$Z_p = \sum_i^{M1} w_{pi} \sum_j^{N1} \| \boldsymbol{p}_{ij}^{\mathrm{DFT}} - \boldsymbol{p}_{ij}^{\mathrm{EIP}} \|^2, \tag{11}$$

where M_1 is the number of ZrO_2 polymorphs and Y_2O_3 for fitting, N_i is the number of atoms contained in the ith crystal structure. E_i^{DFT} and E_i^{EIP} are the DFT and EIP energies, referenced to the energies of the fully relaxed monoclinic ZrO_2. l_{ij}^{DFT} and l_{ij}^{EIP} are the jth DFT and EIP lattice vector components of the ith configuration. $\boldsymbol{p}_{ij}^{\mathrm{DFT}}$ and $\boldsymbol{p}_{ij}^{\mathrm{EIP}}$ are the DFT and EIP fractional coordinates of the jth atom in the ith configuration. w_{e1i}, w_{li} and w_{pi} are the weights of Z_{e1}, Z_l, and Z_p for the ith crystal structure.

Z_{e2}, Z_f, and Z_s are the functions for reproducing the physical response of ZrO_2 and YSZ against atomic displacements and lattice distortions and are defined as follows [40]:

$$Z_{e2} = w_{e2} \frac{\sum_i^{M_2} \left(E_i^{\mathrm{DFT}} - E_i^{\mathrm{EIP}} \right)^2}{M_2 \sum_i^{M_2} \left(E_i^{\mathrm{DFT}} \right)^2}, \tag{12}$$

$$Z_f = w_f \frac{\sum_i^{M2} \sum_j^{Ni} \| \boldsymbol{F}_{ij}^{\mathrm{DFT}} - \boldsymbol{F}_{ij}^{\mathrm{EIP}^2} \|}{\sum_i^{M2} N_i \sum_j^{M2} \| \boldsymbol{F}_{ij}^{\mathrm{DFT}} \|^2}, \tag{13}$$

$$Z_s = w_s \frac{\sum_i^{M_2} \sum_j^{6} \left(S_{ij}^{\mathrm{DFT}} - S_{ij}^{\mathrm{EIP}} \right)^2}{6 M_2 \sum_i^{M_2} \sum_j^{6} \left(S_{ij}^{\mathrm{DFT}} \right)^2}, \tag{14}$$

where M_2 is the number of deformed and MD configurations, N_i is the number of atoms contained in the ith configuration. E_i^{DFT} and E_i^{EIP} are the DFT and EIP energies, referenced to the energies of the fully relaxed configuration (monoclinic ZrO_2 or YSZ models with the lowest energy). $\boldsymbol{F}_{ij}^{\mathrm{DFT}}$ and $\boldsymbol{F}_{ij}^{\mathrm{EIP}}$ are the DFT and EIP force vectors of the jth atom in the ith configuration, and S_{ij}^{DFT} and S_{ij}^{EIP} are the jth DFT and EIP stress tensor components of the ith configuration. w_{e2}, w_f, and w_s are the weights of Z_{e2}, Z_f, and Z_s.

The weights w_{e1i}, w_{li}, w_{pi} were set to 5000, 200, and 500 for monoclinic, tetragonal, and cubic phases, and 500, 20, and 50 for other phases. The weights w_{e2}, w_f, w_s were set to 50000, 1500000, and 30000 (see Discussion S1 for details). For GAOP2, adjustments of w_{e1i} were made to improve the reproducibility of energies for more important (experimentally observed) crystal structures, while reproducing the relative stabilities of various crystal structures, as follows: 2000 for monoclinic, tetragonal, and cubic, 4000 for $SrBr_2$-type structure (mp-775910), 400 for orthorhombic I and II, hy-ZrO_2, and phases with lower energies than the cubic phase in DFT calculation, 20 for others.

2.5. Thermal properties

Phonon band structures and element-projected density of states (DOS) of monoclinic, tetragonal, and cubic ZrO_2 were calculated using

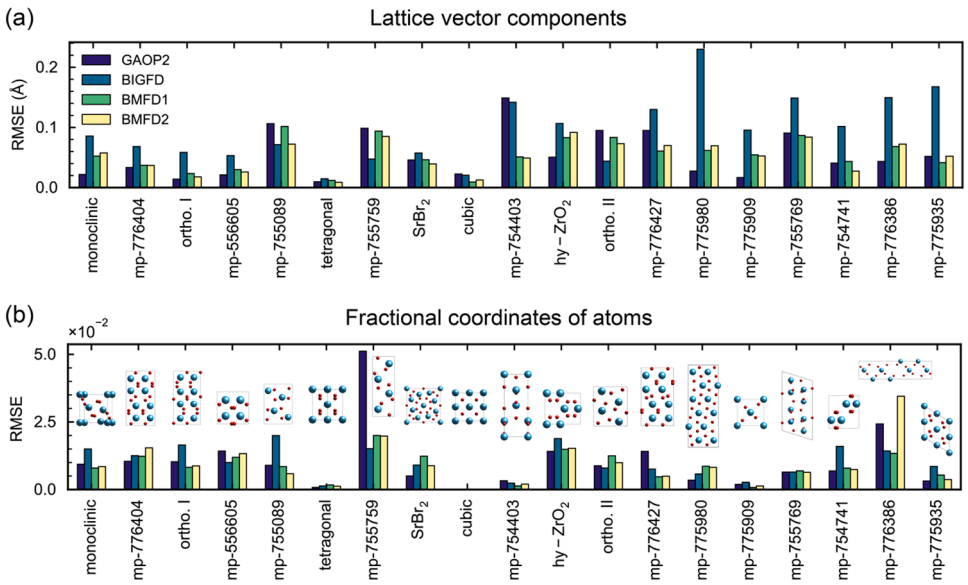

Fig. 2. Reproducibility of crystal structures by EIPs. (a, b) RMSEs of (a) lattice vector components and (b) fractional coordinates of atoms compared with DFT calculations. See subsection 3.1 for the definition of RMSEs. The crystal structures are also shown in (b). Light-blue and red balls represent Zr^{4+} and O^{2-} ions, respectively.

the finite displacement method implemented in Phonopy [49,50]. The second-order force constants were derived from the forces of supercells with an atomic displacement distance of 0.01 Å. For these force calculations, supercells with the cell sizes larger than 10 Å were used to avoid the self-interactions between displaced atoms.

To estimate the temperatures of phase transformations and melting of ZrO_2, MD simulations were performed using the LAMMPS code. We created the supercells of pure tetragonal and monoclinic ZrO_2 and yttria-doped tetragonal YSZ, which have the cell length of approximately 30 Å and contain more than 2500 atoms. For pure ZrO_2, MD simulations were carried out for 5 ns with a timestep of 1 fs (5,000,000 steps), slowly increasing the temperature from 1 to 5000 K. We employed the NPT ensemble using Nosé-Hoover thermostat. For YSZ, the models were heated from 1 to 4000 K in a shorter time of 0.4 ns. Instead, the temperatures of tetragonal-to-cubic phase transformation and melting were averaged among 10 models with random defect configurations for each Y_2O_3 compositions (1.0 - 10.0 mol%).

2.6. Grain boundary structure

We used a rigid-body translation (RBT) approach to find the most energetically stable atomic configuration for a tetragonal GB Σ5(210)/$[001]_{pc}$ for a pseudo-cubic (pc) orientation. Here, [110], [1-10], and [001] orientations in the tetragonal structure correspond to $[100]_{pc}$, $[010]_{pc}$, and $[001]_{pc}$ orientations, respectively. The cell size of the GB models is approximately 46×11×5 Å with the two grain boundaries on the *yz* plane. The models contain 80 Zr and 160 O atoms. Initial GB models were generated by shifting one grain for the directions parallel to the GB plane (*y*- and *z*-axes) and varying the separation of two grains (*x*-axis). The increments of RBTs for *y*- and *z*-axes were 1/4 and 1/8 in fractional coordinates (approximately 1.3 and 1.4 Å, respectively), and the separations between the two grains were set to 0.57, 1.07, and 1.57 Å. By performing structure optimizations for these models, we obtained the energetically stable Σ5(210)/$[001]_{pc}$ GB using DFT and EIP calculations. Note that the orientation of the tetragonal grains may change during the optimization process, and those GBs were excluded from the results. The GB energy ΔE_{GB} of these models was calculated with the following equation [51]:

$$\Delta E_{GB} = \frac{E_{GB} - \frac{N_{GB}}{N_{bulk}} E_{bulk}}{2A}, \tag{15}$$

where E_{bulk} and E_{GB} is the energy of the tetragonal unit cell and the GB model, N_{bulk} and N_{GB} is the number of atoms contained in the unit cell and the GB model, and A is the GB cross-sectional area in the GB model.

For DFT calculations, we optimized the structure of pure tetragonal ZrO_2 unit cell with a plane-wave energy cutoff of 550 eV to obtain the lattice constants with high precision. The structure optimizations of GB models were performed with a lower energy cutoff of 420 eV and fixed lattice constants, to reduce the computational cost. The first Brillouin zone was sampled with Monkhorst-Pack *k*-point grids of 1×2×4 [47]. To accurately calculate the GB energy, a DFT calculation was rerun for the lowest energy GB model with the plane-wave energy cutoff of 550 eV, where the cell shape and size were optimized including the direction perpendicular to the GB.

3. Results and Discussion

3.1. Developed potentials

Fig. 1(a) compares the relative energies of ZrO_2 polymorphs in DFT calculations and classical force field calculations using the developed GAOP1 (see Table 1 for the parameters). The ZrO_2 polymorphs include monoclinic, tetragonal, cubic, orthorhombic I and II phases as well as various hypothetical structures taken from the Materials Project database. In Fig. 1(a), the plotted points are aligned on the black line, indicating that the relative energies (stabilities) of the ZrO_2 polymorphs are well reproduced by GAOP1. Notably, the order of stability is reproduced for the experimentally observed crystal structures, namely monoclinic, tetragonal, cubic, and orthorhombic I and II structures. The largest deviation from the DFT calculation is in the structure of mp-754751, which has an oxygen polyhedron of trigonal prism [52]. For this structure, other EIPs also have significantly larger energies than that of the DFT calculation as seen in Fig. 1(b-f), suggesting that EIPs based on the Coulomb-Buckingham potential are difficult to reproduce the stability of this crystal structure. The most severe computational problem with GAOP1 is that the $SrBr_2$-type structure is predicted to be too stable. The DFT calculations show that this structure has an energy between tetragonal and cubic phases, but it is the second most stable

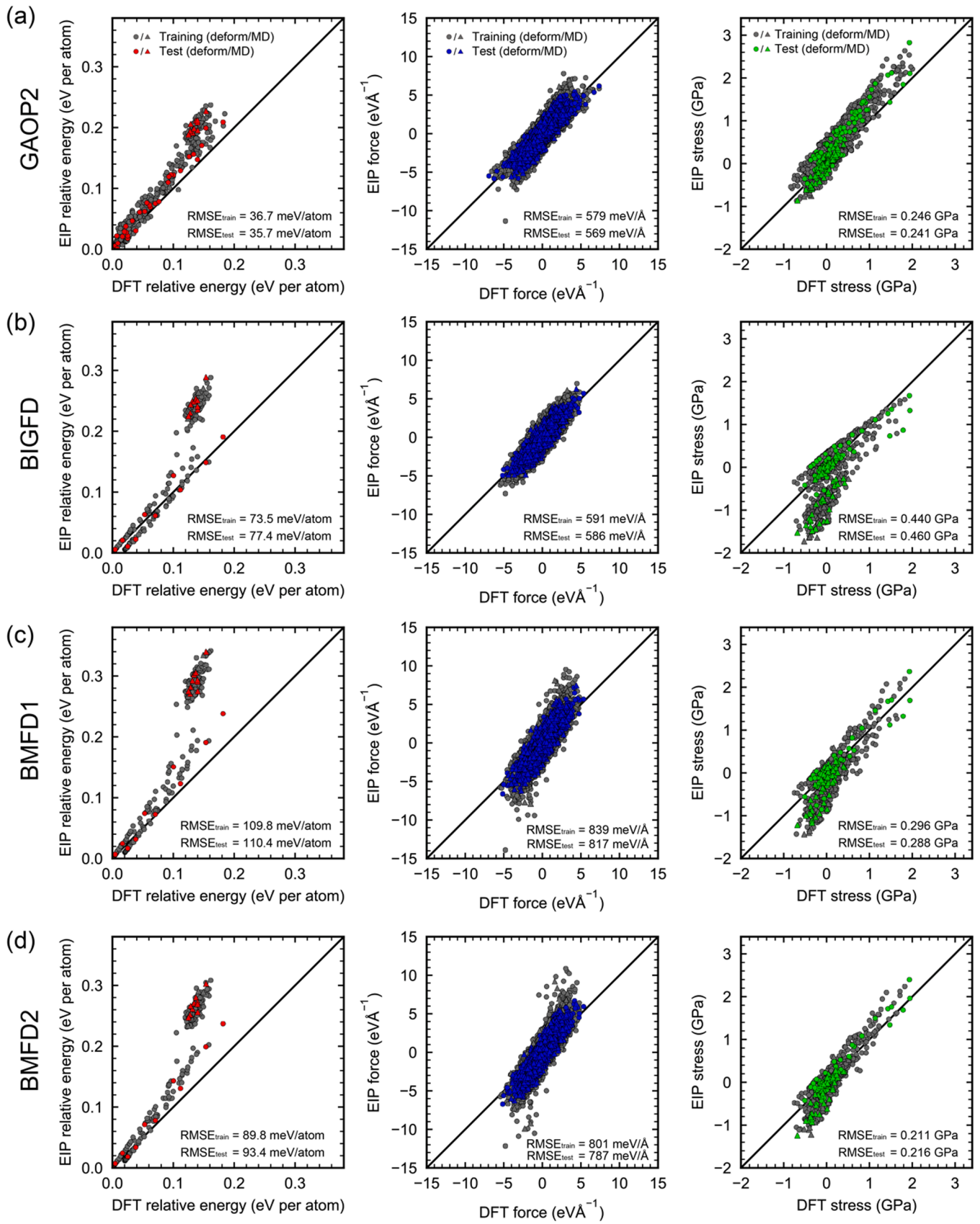

Fig. 3. Comparison of energies, forces, and stresses calculated using the EIPs and DFT. (a) The developed GAOP2. (b-d) The potentials reported by Bandura et al. [38], namely (b) BIGFD, (c) BMFD1, and (d) BMFD2. The values calculated from the models used for the GAOP2 training and testing are plotted with gray and colored points, respectively. The diagonal line means that the values calculated by the EIPs and DFT are equal. The RMSEs of energies, forces, and stresses are also indicated in the panels.

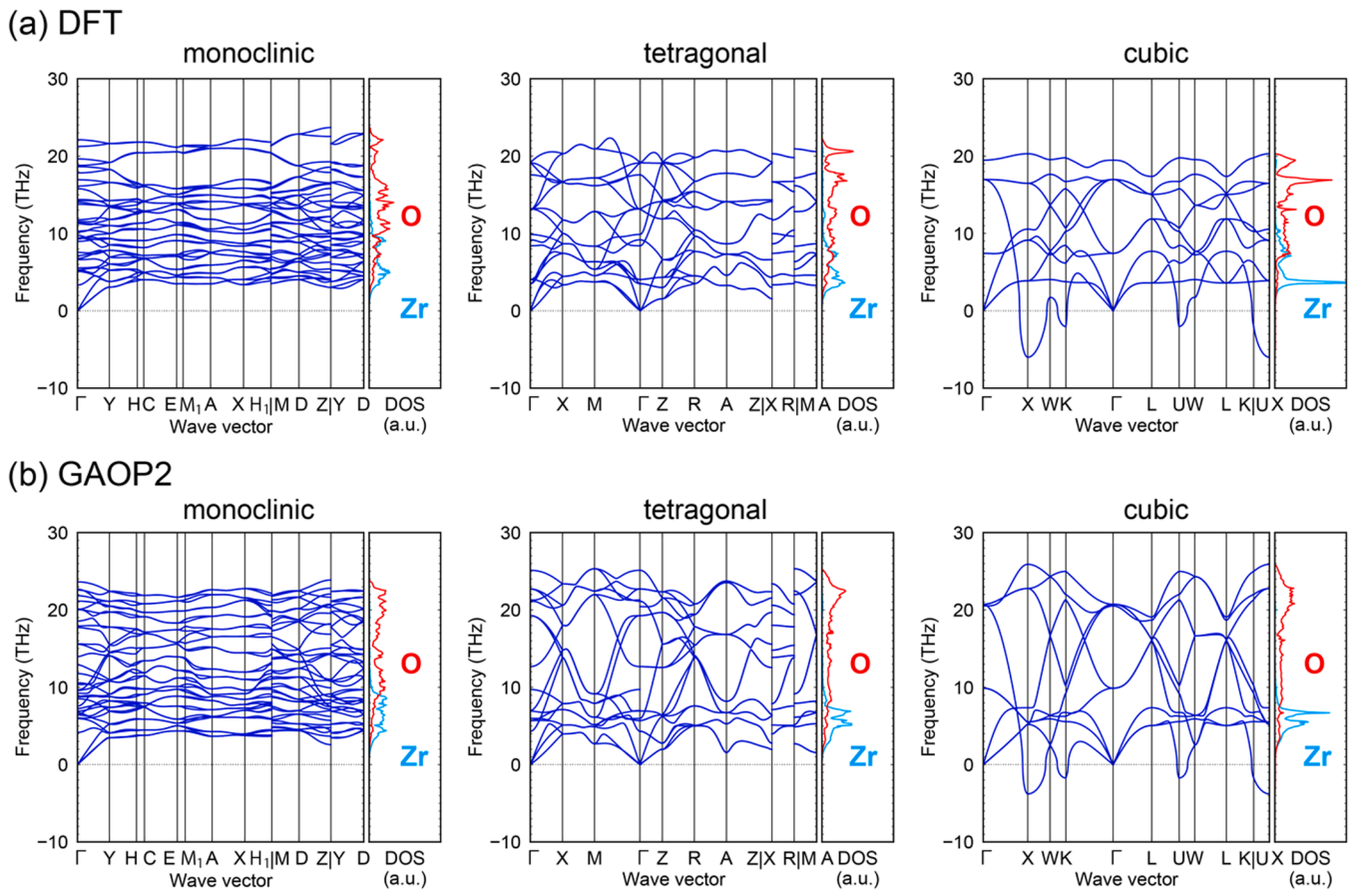

Fig. 4. Phonon band structures and element-projected phonon density of states for monoclinic, tetragonal, and cubic ZrO_2 obtained by (a) DFT calculations and (b) GAOP2. The negative number of the vertical axis indicates imaginary frequency.

structure after the monoclinic phase in GAOP1. Since this $SrBr_2$-type structure is a unique structure that may appear at tetragonal grain boundaries as discussed later, the overestimation of the stability for this structure may cause problems in searches of lattice defect structures.

To reproduce the order of phase stability more accurately, we created GAOP2 optimized with the training data including the energies and structures of 19 ZrO_2 polymorphs (see Table 2 for the parameters). The relative energies obtained using GAOP2 are shown in Fig. 1(b). Although the energies were estimated lower than those of the DFT calculations, relative energies (stabilities) of ZrO_2 polymorphs were more precisely reproduced, except for mp-754741.

The reproducibility of phase stability was also evaluated for four other EIPs considering multiple ZrO_2 phases. Using the simple Coulomb-Buckingham potential reported by Schelling *et al.*[37], the relative stabilities of ZrO_2 polymorphs were not successfully reproduced, with some crystal structures having lower energies than the monoclinic phase (Fig. 1(c)). A few structures were transformed to other crystal structures during the structural optimization. The three EIPs reported by Bandura *et al.* (called BIGFD, BMFD1, and BMFD2) [38], in which the Coulomb-Buckingham potential was combined with several additional potential functions, were found to have a monoclinic structure as the most stable phase (Fig. 1(d)-(f)). The phase stability of the ZrO_2 polymorphs was also well reproduced by the three EIPs, especially by BMFD1, but there were a few phases with the overestimated energies than by GAOP2. These comparisons indicate that the GAOP2 developed in this study performs better than the previous EIPs in terms of reproducing the relative stability of the ZrO_2 polymorphs.

The reproducibility of ZrO_2 structures were compared between GAOP2, BIGFD, BMFD1, and BMFD2 (Fig. 2). The root mean squared errors (RMSEs) of the lattice vectors and fractional coordinates of atoms were defined as follows:

$$\text{RMSE (lattice vector)} = \sqrt{\sum_{i}^{6} \left(l_i^{\text{EIP}} - l_i^{\text{DFT}}\right)^2 \Big/ 6}, \tag{16}$$

$$\text{RMSE (atom coordinate)} = \sqrt{\sum_{i}^{N} \|\boldsymbol{p}_i^{\text{EIP}} - \boldsymbol{p}_i^{\text{DFT}}\|^2 \Big/ 3N}, \tag{17}$$

where l_i^{EIP} and l_i^{DFT} are the ith EIP and DFT lattice vector components, $\boldsymbol{p}_i^{\text{EIP}}$ and $\boldsymbol{p}_i^{\text{DFT}}$ and are the EIP and DFT fractional coordinates of the ith atom, and N is the number of atoms in a ZrO_2 structure. The lattice vectors are in good agreement with the DFT calculations for all EIPs, with RMSEs of 0.15 Å or less, except for the mp-775980 structure with BIGFD. For the fractional atomic coordinates (with the values between 0 and 1), the RMSEs were less than 0.02 in most cases, with no significant discrepancies. The large deviation was seen in the structure of mp-755759, with the RMSE of ~ 0.05 in GAOP2. This is because the structure transformed into a tetragonal structure during the structural optimization, although this transformation was not observed for other three EIPs. This is a drawback of GAOP2, but it was found that a wide variety of ZrO_2 structures can be reproduced by GAOP2 and other three EIPs.

The energies, forces acting on atoms, and stresses for the deformed cubic and tetragonal structures and MD tetragonal structures were compared between the DFT and EIP calculations (Fig. 3). The energies, forces, and stresses have a significant impact on the dynamical structural stability and the reproducibility of the physical properties such as mechanical and thermal properties. Note that only GAOP2 contains the data of 3YSZ and 10YSZ, because the other EIPs do not include the

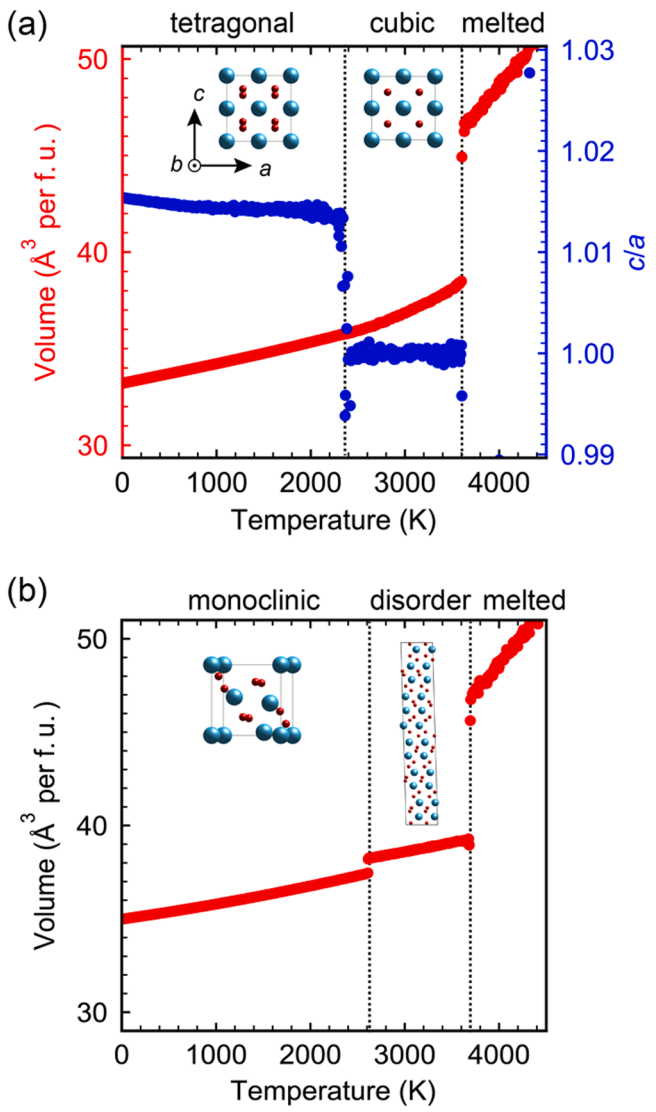

Fig. 5. Volume and c/a ratio of ZrO_2 as a function of temperature, starting from the structures of (a) tetragonal and (b) monoclinic phases. GAOP2 was used for the calculation.

potentials for yttrium (see **Fig. S1** for plots that separately show the data of ZrO_2 and YSZ in GAOP2). As shown in Fig. 3, GAOP2 showed the lowest RMSEs of the four EIPs in energy, force, and stress. The RMSE for the training and test datasets were comparable, indicating that no overfitting occurred. For the other EIPs, the errors were more pronounced for the significantly deformed models and MD structures. The energies were overestimated by the three EIPs, with large errors in stress for BIGFD and in force for BMFD1 and BMFD2. This comparison shows that GAOP2 has a better reproducibility of energy, force, and stress in tetragonal and cubic phases compared with the other EIPs. In summary, the developed GAOP2 are the potentials that sufficiently reproduces the relative stability, crystal structures, and responses to structural deformation.

3.2. Phase stability and thermal properties

Fig. 4 shows phonon band structures and element-projected phonon DOS for the monoclinic, tetragonal, and cubic phases that are of practical importance, calculated by DFT and GAOP2 calculations. The shape of phonon dispersions seems to be consistent between GAOP2 and DFT calculations, although the phonon frequencies are overestimated, and

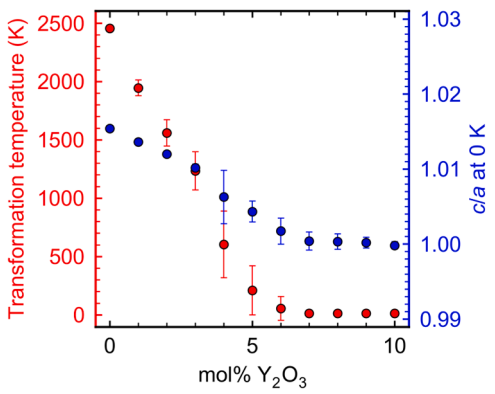

Fig. 6. Transformation temperature from cubic to tetragonal phase and c/a ratio at 0 K as a function of Y_2O_3 concentration. GAOP2 was used for the calculations. Bars indicate the standard deviation of transformation temperature or c/a ratio among 10 models with different defect configurations.

optical phonon modes are more dispersive in GAOP2 (see **Fig. S2** for possible reasons). In particular, the monoclinic and tetragonal phases are dynamically stable, and the imaginary mode of the cubic phase that indicates the spontaneous transformation from the cubic phase to the tetragonal phase is reproduced. This result demonstrates that GAOP2 can reproduce the dynamical stability of monoclinic, tetragonal, and cubic phases at 0 K.

To investigate the stability of the tetragonal and cubic phases under finite temperature, the tetragonal phase was heated from 1 K to 5000 K by MD simulations using GAOP2. Fig. 5(a) shows the change in lattice volume and the lattice parameter ratio c/a during the temperature increase (Here a pseudo cubic structure is considered for the length of a- and c- axes as seen in the inset of Fig. 5(a)). The tetragonal structure thermally expanded while maintaining the c/a ratio of about 1.015, which is underestimated compared to the experimental ratio of ~1.025 [53]. The calculated linear coefficients of thermal expansion (CTE) at 1200 - 1800 K are 10.7×10^{-6} K^{-1} for a-axis and 10.9×10^{-6} K^{-1} for c-axis, which are consistent with the experimental values (~11×10^{-6} K^{-1} for a-axis and ~15×10^{-6} K^{-1} for c-axis) [54]. The tetragonal phase was transformed to the cubic phase at about 2380 K. This transformation temperature is slightly underestimated compared to the experimentally reported temperature of ~ 2570 K [53], but agreed well with the 2386 K determined by an MLP [28]. Further heating of the cubic phase resulted in melting at about 3600 K, overestimated compared to the experimental value of ~3000 K [8]. By using BIGFD, BMFD1, and BMFD2, the c/a ratio decreased rapidly with increasing temperature, and the tetragonal phase transformed to the cubic phase at temperatures between 100 and 900 K (**Figs. S3-5**). The melting points were above 4000 K, and the cubic phase did not melt even at 5000 K in BMFD2. These results indicate that GAOP2 is the only EIP capable of reproducing the dynamic behaviors of tetragonal and cubic phases in the high temperature range.

We also performed similar MD simulations to investigate the structural stability of the monoclinic phase under finite temperature (Fig. 5 (b)). The monoclinic phase remained until 2610 K in GAOP2, after which it transformed into a disorder phase with a mixture of different coordination environments. The monoclinic-to-tetragonal transformation was not observed in GAOP2, although it has experimentally been reported at 1400-1500 K [53]. This may be attributed to the fact that the deformed and MD structures of the monoclinic phase were not included in the training dataset. However, it should be noted that including such data may reduce the reproducibility of other structures and properties (see Discussion S1). The transformation to the disorder phase is possibly because the monoclinic phase could not transform completely to one of the structures shown in Fig. 2(b), due to the mismatch in cell geometry or number of atoms contained in the supercell. Similarly, the EIPs of BIGFD, BMFD1, and BMFD2 cannot reproduce

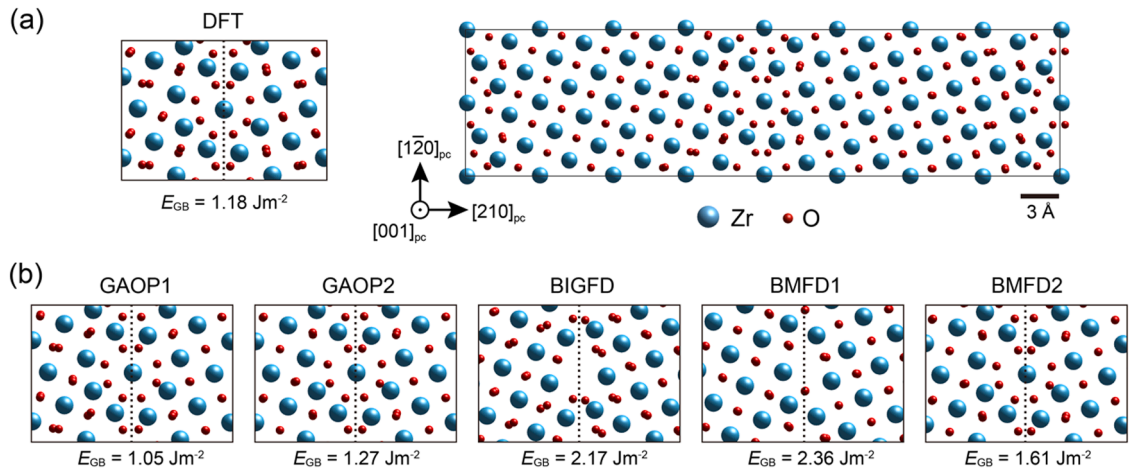

Fig. 7. (a) The most stable structure of a tetragonal grain boundary Σ5(210)/[001]$_{pc}$ obtained by the DFT calculations. (b) The respective structures of Σ5(210)/[001]$_{pc}$ obtained by EIPs. The grain boundary energies E_{GB} are also shown.

transformation from the monoclinic to the tetragonal phase, but a transition from monoclinic to cubic phase, where the tetragonal phase was skipped, occurred at high temperatures above 3000 K (**Figs. S3-5**).

The stability of tetragonal and cubic structures in YSZ was also investigated by MD simulations with GAOP2. Fig. 6 shows the temperature of the tetragonal-to-cubic phase transformation and the *c/a* ratio at 0 K, as a function of mol% Y_2O_3. Both decreased linearly with increasing yttria content, and the cubic phase was formed even at 0 K when Y_2O_3 mol% reached 7%. The experimental trends of the tetragonal structure at low mol% Y_2O_3 and the cubic structure at high mol% Y_2O_3 are well reproduced by GAOP2. The mol% Y_2O_3 at which the cubic structure is formed is close to the experimental results (8-10 mol% Y_2O_3) [9]. The reproducibility of the relative stability of the tetragonal and cubic phases in YSZ is considerably improved by GAOP2, since the Schelling potential shows that YSZ is cubic at 0 K with 4 mol% Y_2O_3 [37]. Upon further heating, YSZ expanded while maintaining its cubic structure until melting. The melting point decreased with increasing yttria content and reached about 3150 K for 8YSZ (**Fig. S6**). The melting point is in good agreement with experimental results, although the decrease in melting point is not observed for mol% Y_2O_3 below 10% in the experiments [7,9]. In summary, GAOP2 is an EIP that can simulate monoclinic, tetragonal, and cubic ZrO_2 as well as tetragonal and cubic YSZ even at finite temperature, although the reproducibility of the monoclinic-to-tetragonal phase transformation is limited.

3.3. Application to a tetragonal grain boundary

Finally, as an application of the constructed GAOP2, we explored the structure of a GB in the tetragonal phase by rigid body translations. Fig. 7(a) shows the most stable GB structure of Σ5(210)/[001]$_{pc}$ obtained by DFT calculations. At the GB plane, a local coordination environment similar to the $SrBr_2$-type structure was formed (see Fig. 2(b)). The most stable GB structures obtained by EIPs (GAOP1, GAOP2, BIGFD, BMFD1, and BMFD2) are also shown in Fig. 7(b). The $SrBr_2$-type local coordination environment is reproduced by GAOP1, GAOP2, and BMFD2, although there are slight structure differences from DFT calculations, especially in the positions of oxide ions about 6Å away from the GB plane. With BIGFD and BMFD1, no $SrBr_2$-type structures were found by the search under the same conditions, but the structure optimization started with the most stable DFT structure yielded lower GB energies than those in Fig. 7(b) (1.61 Jm^{-2} for BIGFD and 1.58 Jm^{-2} for BMFD1). The GB energy for GAOP2 is closest to the DFT calculation, probably reflecting the high reproducibility of phase stability as shown in Fig. 1. GAOP1 has a lower grain boundary energy than the DFT calculation, presumably due to the underestimated energy of $SrBr_2$-type structure, which is improved in GAOP2. The cation arrangements in cubic YSZ observed by the scanning transmission electron microscopy (STEM) [25] are different from the $SrBr_2$-type structure shown in Fig. 7. This indicates that the $SrBr_2$-type structure may be the coordination environment that occurs specifically at tetragonal GBs. The agreement with the DFT calculations demonstrates that GAOP2 can be used to explore the GB structures of the tetragonal phase due to its ability to reproduce the structures and stabilities of ZrO_2 polymorphs.

4. Conclusions

We have developed an empirical interatomic potential GAOP2 optimized for various ZrO_2 polymorphs and the solid solution system of YSZ, including monoclinic, tetragonal, and cubic phases that are of practical importance. GAOP2 can reproduce the relative stability of ZrO_2 polymorphs at 0K, energies, forces acting on atoms, and stresses in the tetragonal and cubic phases, and the temperature and yttria concentration dependence of tetragonal-cubic stability, as well as the thermal properties. It was also found that the structure of a tetragonal grain boundary Σ5(210)/[001]$_{pc}$ derived by GAOP2 is consistent with that obtained by DFT calculations. The developed potential will allow us to systematically explore tetragonal grain boundary structures, yttria segregation behavior, complex defect configurations in tetragonal and cubic YSZ, and their impact on mechanical and thermal properties.

Data availability

The data that support the findings of this study are available from the corresponding author upon reasonable request.

Declaration of Competing Interest

The authors declare that they have no known competing financial interests or personal relationships that could have appeared to influence the work reported in this paper.

Acknowledgements

A part of this study was supported by Next Generation Zirconia Social Cooperation Program, The University of Tokyo. This work was also supported by Grants-in-Aid for Early-Career Scientists [grant numbers JP20K15034, JP23K13544], Grants-in-Aid for Scientific Research on Innovative Areas [grant numbers JP20H05195, JP19H05786], and Grant-in-Aid for Transformative Research Areas [grant number JP22H05146] from the Japan Society for the Promotion of Science

(JSPS).

Supplementary materials

Supplementary material associated with this article can be found, in the online version, at doi:10.1016/j.actamat.2023.119460.

References

[1] B. Basu, Toughening of yttria-stabilised tetragonal zirconia ceramics, Int. Mater. Rev. 50 (2005) 239–256, https://doi.org/10.1179/174328005x41113.

[2] K. Matsui, H. Yoshida, Y. Ikuhara, Review: microstructure-development mechanism during sintering in polycrystalline zirconia, Int. Mater. Rev. 63 (2018) 375–406, https://doi.org/10.1080/09506608.2017.1402424.

[3] J. Chevalier, A. Liens, H. Reveron, F. Zhang, P. Reynaud, T. Douillard, L. Preiss, V. Sergo, V. Lughi, M. Swain, N. Courtois, Forty years after the promise of «ceramic steel?»: Zirconia-based composites with a metal-like mechanical behavior, J. Am. Ceram. Soc. 103 (2020) 1482–1513, https://doi.org/10.1111/jace.16903.

[4] N.P. Padture, Thermal Barrier Coatings for Gas-Turbine Engine Applications, Science 296 (80) (2002) 280–284, https://doi.org/10.1126/science.1068609.

[5] B.C.H. Steele, A. Heinzel, Materials for fuel-cell technologies, Nature 414 (2001) 345–352, https://doi.org/10.1038/35104620.

[6] J.R. Kelly, I. Denry, Stabilized zirconia as a structural ceramic: An overview, Dent. Mater. 24 (2008) 289–298, https://doi.org/10.1016/j.dental.2007.05.005.

[7] H.G. Scott, Phase relationships in the zirconia-yttria system, J. Mater. Sci. 10 (1975) 1527–1535, https://doi.org/10.1007/BF01031853.

[8] O.R.J. Ackermann, S.P. Garg, E.G. Rauh, High-Temperature Phase Diagram for the System Zr-O, J. Am. Ceram. Soc. 60 (1977) 341–345, https://doi.org/10.1111/j.1151-2916.1977.tb15557.x.

[9] M. Jayaratna, M. Yoshimura, S. Somiya, Subsolidus Phase Relations in the Pseudoternary System ZrO_2-$YO_{1.5}$-$CrO_{1.5}$ in Air, J. Am. Ceram. Soc. 67 (1984), https://doi.org/10.1111/j.1151-2916.1984.tb19496.x c240–c242.

[10] P. Li, I.-W Chen, J.E. Penner-Hahn, Effect of Dopants on Zirconia Stabilization—An X-ray Absorption Study: I, Trivalent Dopants, J. Am. Ceram. Soc. 77 (1994) 118–128, https://doi.org/10.1111/j.1151-2916.1994.tb06964.x.

[11] P. Li, I.-W Chen, J.E. Penner-Hahn, Effect of Dopants on Zirconia Stabilization—An X-ray Absorption Study: II, Tetravalent Dopants, J. Am. Ceram. Soc. 77 (1994) 1281–1288, https://doi.org/10.1111/j.1151-2916.1994.tb05403.x.

[12] K. Matsui, K. Hosoi, B. Feng, H. Yoshida, Y. Ikuhara, Ultrahigh toughness zirconia ceramics, Proc. Natl. Acad. Sci. 120 (2023), e2304498120, https://doi.org/10.1073/pnas.2304498120.

[13] K. Matsui, N. Ohmichi, M. Ohgai, H. Yoshida, Y. Ikuhara, Grain boundary segregation-induced phase transformation in yttria-stabilized tetragonal zirconia polycrystal, J. Ceram. Soc. Japan. 114 (2006) 230–237, https://doi.org/10.2109/jcersj.114.230.

[14] R.C. Garvie, R.H. Hannink, R.T. Pascoe, Ceramic steel? Nature 258 (1975) 703–704, https://doi.org/10.1038/258703a0.

[15] J.A. Krogstad, S. Krämer, D.M. Lipkin, C.A. Johnson, D.R.G. Mitchell, J.M. Cairney, C.G. Levi, Phase stability of t′-zirconia-based thermal barrier coatings: Mechanistic insights, J. Am. Ceram. Soc. 94 (2011), https://doi.org/10.1111/j.1551-2916.2011.04531.x s168–s177.

[16] H. Masuda, K. Morita, M. Watanabe, T. Hara, H. Yoshida, T. Ohmura, Ferroelastic and plastic behaviors in pseudo-single crystal micropillars of nontransformable tetragonal zirconia, Acta Mater 203 (2021), 116471, https://doi.org/10.1016/j.actamat.2020.11.013.

[17] C. Ahamer, A.K. Opitz, G.M. Rupp, J. Fleig, Revisiting the Temperature Dependent Ionic Conductivity of Yttria Stabilized Zirconia (YSZ), J. Electrochem. Soc. 164 (2017) F790–F803, https://doi.org/10.1149/2.0641707jes.

[18] T. Oyama, M. Yoshiya, H. Matsubara, K. Matsunaga, Numerical analysis of solute segregation at Σ5 (310)/[001]symmetric tilt grain boundaries in Y_2O_3-doped ZrO_2, Phys. Rev. B - Condens. Matter Mater. Phys. 71 (2005), 224105, https://doi.org/10.1103/PhysRevB.71.224105.

[19] T. Yokoi, M. Yoshiya, H. Yasuda, On modeling of grain boundary segregation in aliovalent cation doped ZrO_2: Critical factors in site-selective point defect occupancy, Scr. Mater. 102 (2015) 91–94, https://doi.org/10.1016/j.scriptamat.2015.02.021.

[20] B. Feng, T. Yokoi, A. Kumamoto, M. Yoshiya, Y. Ikuhara, N. Shibata, Atomically ordered solute segregation behaviour in an oxide grain boundary, Nat. Commun. 7 (2016) 11079, https://doi.org/10.1038/ncomms11079.

[21] M. Jaipal, A. Chatterjee, Effect of the Σ5(310)/[001]tilt grain boundary on oxygen-ion movement in yttria-stabilized zirconia: Insights from molecular dynamics, Acta Mater 165 (2019) 307–314, https://doi.org/10.1016/j.actamat.2018.11.064.

[22] J.C. Madrid Madrid, J. Matsuda, K. Leonard, H. Matsumoto, K.K. Ghuman, Molecular dynamics study of oxygen-ion diffusion in yttria-stabilized zirconia grain boundaries, J. Mater. Chem. A. 10 (2022) 2567–2579, https://doi.org/10.1039/d1ta08309k.

[23] Y. Ikuhara, P. Thavorniti, T. Sakuma, Solute segregation at grain boundaries in superplastic SiO2-doped TZP, Acta Mater 45 (1997) 5275–5284, https://doi.org/10.1016/S1359-6454(97)00152-3.

[24] K. Matsui, H. Yoshida, Y. Ikuhara, Nanocrystalline, ultra-degradation-resistant zirconia: Its grain boundary nanostructure and nanochemistry, Sci. Rep. 4 (2014) 4758, https://doi.org/10.1038/srep04758.

[25] B. Feng, N.R. Lugg, A. Kumamoto, Y. Ikuhara, N. Shibata, Direct Observation of Oxygen Vacancy Distribution across Yttria-Stabilized Zirconia Grain Boundaries, ACS Nano 11 (2017) 11376–11382, https://doi.org/10.1021/acsnano.7b05943.

[26] K. Parlinski, Z. Li, Y. Kawazoe, First-principles determination of the soft mode in cubic ZrO_2, Phys. Rev. Lett. 78 (1997) 4063–4066, https://doi.org/10.1103/PhysRevLett.78.4063.

[27] A. Kuwabara, T. Tohei, T. Yamamoto, I. Tanaka, Ab initio lattice dynamics and phase transformations of ZrO_2, Phys. Rev. B - Condens. Matter Mater. Phys. 71 (2005), 064301, https://doi.org/10.1103/PhysRevB.71.064301.

[28] C. Verdi, F. Karsai, P. Liu, R. Jinnouchi, G. Kresse, Thermal transport and phase transitions of zirconia by on-the-fly machine-learned interatomic potentials, Npj Comput. Mater. 7 (2021) 156, https://doi.org/10.1038/s41524-021-00630-5.

[29] P. Liu, C. Verdi, F. Karsai, G. Kresse, Phase transitions of zirconia: Machine-learned force fields beyond density functional theory, Phys. Rev. B. 105 (2022), https://doi.org/10.1103/PhysRevB.105.L060102. L060102.

[30] R. Ganser, S. Bongarz, A. Von Mach, L. Azevedo Antunes, A. Kersch, Piezo- and Pyroelectricity in Zirconia: A Study with Machine-Learned Force Fields, Phys. Rev. Appl. 18 (2022), 054066, https://doi.org/10.1103/PhysRevApplied.18.054066.

[31] S.H. Guan, K.X. Zhang, C. Shang, Z.P. Liu, Stability and anion diffusion kinetics of Yttria-stabilized zirconia resolved from machine learning global potential energy surface exploration, J. Chem. Phys. 152 (2020), 094703, https://doi.org/10.1063/1.5142591.

[32] S.H. Guan, C. Shang, Z.P. Liu, Resolving the Temperature and Composition Dependence of Ion Conductivity for Yttria-Stabilized Zirconia from Machine Learning Simulation, J. Phys. Chem. C. 124 (2020) 15085–15093, https://doi.org/10.1021/acs.jpcc.0c04331.

[33] S. Fujii, A. Seko, Structure and lattice thermal conductivity of grain boundaries in silicon by using machine learning potential and molecular dynamics, Comput. Mater. Sci. 204 (2022), 111137, https://doi.org/10.1016/j.commatsci.2021.111137.

[34] A. Seko, Machine learning potentials for multicomponent systems: The Ti-Al binary system, Phys. Rev. B. 102 (2020), 174104, https://doi.org/10.1103/PhysRevB.102.174104.

[35] P. Friederich, F. Häse, J. Proppe, A. Aspuru-Guzik, Machine-learned potentials for next-generation matter simulations, Nat. Mater. 20 (2021) 750–761, https://doi.org/10.1038/s41563-020-0777-6.

[36] G.V. Lewis, C.R.A. Catlow, Potential models for ionic oxides, J. Phys. C Solid State Phys. 18 (1985) 1149–1161, https://doi.org/10.1088/0022-3719/18/6/010.

[37] P.K. Schelling, S.R. Phillpot, D. Wolf, Mechanism of the Cubic-to-Tetragonal Phase Transition in Zirconia and Yttria-Stabilized Zirconia by Molecular-Dynamics Simulation, J. Am. Ceram. Soc. 84 (2001) 1609–1619, https://doi.org/10.1111/j.1151-2916.2001.tb00885.x.

[38] A.V. Bandura, S.I. Lukyanov, R.A. Evarestov, Atom–atom force field for simulation of zirconia bulk, nanosheets and nanotubes, Mol. Simul. 43 (2017) 886–899, https://doi.org/10.1080/08927022.2017.1303685.

[39] O. Ohtaka, H. Fukui, T. Kunisada, T. Fujisawa, K. Funakoshi, W. Utsumi, T. Irifune, K. Kuroda, T. Kikegawa, Phase relations and equations of state of ZrO_2 under high temperature and high pressure, Phys. Rev. B - Condens. Matter Mater. Phys. 63 (2001), 174108, https://doi.org/10.1103/PhysRevB.63.174108.

[40] A. Rohskopf, H.R. Seyf, K. Gordiz, T. Tadano, A. Henry, Empirical interatomic potentials optimized for phonon properties, Npj Comput. Mater. 3 (2017) 27, https://doi.org/10.1038/s41524-017-0026-y.

[41] A. Jain, S.P. Ong, G. Hautier, W. Chen, W.D. Richards, S. Dacek, S. Cholia, D. Gunter, D. Skinner, G. Ceder, K.A. Persson, Commentary: The materials project: A materials genome approach to accelerating materials innovation, APL Mater 1 (2013), 011002, https://doi.org/10.1063/1.4812323.

[42] A. Seko, A. Togo, I. Tanaka, Group-theoretical high-order rotational invariants for structural representations: Application to linearized machine learning interatomic potential, Phys. Rev. B. 99 (2019), 214108, https://doi.org/10.1103/PhysRevB.99.214108.

[43] P.E. Blöchl, Projector augmented-wave method, Phys. Rev. B. 50 (1994) 17953–17979, https://doi.org/10.1103/PhysRevB.50.17953.

[44] G. Kresse, J. Hafner, Ab initio molecular-dynamics simulation of the liquid-metal–amorphous-semiconductor transition in germanium, Phys. Rev. B. 49 (1994) 14251–14269, https://doi.org/10.1103/PhysRevB.49.14251.

[45] G. Kresse, J. Furthmüller, Efficient iterative schemes for ab initio total-energy calculations using a plane-wave basis set, Phys. Rev. B. 54 (1996) 11169–11186, https://doi.org/10.1103/PhysRevB.54.11169.

[46] J.P. Perdew, A. Ruzsinszky, G.I. Csonka, O.A. Vydrov, G.E. Scuseria, L. A. Constantin, X. Zhou, K. Burke, Restoring the density-gradient expansion for exchange in solids and surfaces, Phys. Rev. Lett. 100 (2008), 136406, https://doi.org/10.1103/PhysRevLett.100.136406.

[47] H.J. Monkhorst, J.D. Pack, Special points for Brillouin-zone integrations, Phys. Rev. B. 13 (1976) 5188–5192, https://doi.org/10.1103/PhysRevB.13.5188.

[48] S. Plimpton, Fast Parallel Algorithms for Short-range molecular dynamics, J. Comput. Phys. 117 (1995) 1–19, https://doi.org/10.1006/jcph.1995.1039.

[49] A. Togo, I. Tanaka, First principles phonon calculations in materials science, Scr. Mater. 108 (2015) 1–5, https://doi.org/10.1016/j.scriptamat.2015.07.021.

[50] A. Togo, First-principles Phonon Calculations with Phonopy and Phono3py, J. Phys. Soc. Japan. 92 (2023), 012001, https://doi.org/10.7566/JPSJ.92.012001.

[51] S. Fujii, T. Yokoi, M. Yoshiya, Atomistic mechanisms of thermal transport across symmetric tilt grain boundaries in MgO, Acta Mater 171 (2019) 154–162, https://doi.org/10.1016/j.actamat.2019.04.009.

[52] D. Waroquiers, X. Gonze, G.M. Rignanese, C. Welker-Nieuwoudt, F. Rosowski, M. Göbel, S. Schenk, P. Degelmann, R. André, R. Glaum, G. Hautier, Statistical

analysis of coordination environments in Oxides, Chem. Mater. 29 (2017) 8346–8360, https://doi.org/10.1021/acs.chemmater.7b02766.
[53] P. Aldebert, J.-P Traverse, Structure and Ionic Mobility of Zirconia at High Temperature, J. Am. Ceram. Soc. 68 (1985) 34–40, https://doi.org/10.1111/j.1151-2916.1985.tb15247.x.
[54] R.P. Haggerty, P. Sarin, Z.D. Apostolov, P.E. Driemeyer, W.M. Kriven, Thermal expansion of HfO_2 and ZrO_2, J. Am. Ceram. Soc. 97 (2014) 2213–2222, https://doi.org/10.1111/jace.12975.